

# 1-D ELECTRICAL INVERSION SENSITIVITY APPLIED TO CO<sub>2</sub> GEOLOGICAL STORAGE MONITORING

Amin BASSREI

## ABSTRACT

Discussions on the effects of anthropogenic emissions of greenhouse gas and their consequences on climate change have gained public notoriety in recent decades. The capture of carbon dioxide (CO<sub>2</sub>) from industrial sources and its subsequent storage in geological reservoirs has the potential to play an important role in reducing the harmful effects of the atmosphere CO<sub>2</sub> emissions in the medium and long term. Based on their physical properties for applying geophysical techniques, studying and evaluating the behavior of rocks in the presence of CO<sub>2</sub> has shown high relevance. This study deals with monitoring geological reservoirs in the presence of CO<sub>2</sub> through the electrical resistivity method to estimate the electrical properties of the rocks involved, such as CO<sub>2</sub> saturation and electrical resistivity of the medium. Simulations were performed on a four-layer synthetic model. The results validated the applicability of the electrical method in monitoring CO<sub>2</sub> injection and leakage.

*Keywords:* CO<sub>2</sub> geological storage; Climate change; Electrical forward modeling; Inversion of electrical resistivity data.

## RESUMO

SENSIBILIDADE DA INVERSÃO ELÉTRICA 1-D APLICADA AO MONITORAMENTO DO ARMAZENAMENTO GEOLÓGICO DE CO<sub>2</sub>. As discussões sobre os efeitos das emissões antrópicas de gases de efeito estufa e suas consequências nas mudanças climáticas ganharam notoriedade pública nas últimas décadas. A captura de dióxido de carbono (CO<sub>2</sub>) de fontes industriais e seu posterior armazenamento em reservatórios geológicos tem o potencial de desempenhar um papel importante na redução dos efeitos nocivos das emissões de CO<sub>2</sub> da atmosfera a médio e longo prazo. Com base em suas propriedades físicas para aplicação de técnicas geofísicas, o estudo e a avaliação do comportamento de rochas na presença de CO<sub>2</sub> tem se mostrado de alta relevância. Este estudo trata do monitoramento de reservatórios geológicos na presença de CO<sub>2</sub> por meio do método da resistividade elétrica para estimar as propriedades elétricas das rochas envolvidas, como saturação de CO<sub>2</sub> e resistividade elétrica do meio. As simulações foram realizadas em um modelo sintético de quatro camadas. Os resultados validaram a aplicabilidade do método elétrico para o monitoramento da injeção e vazamento de CO<sub>2</sub>.

*Palavras-chave:* Armazenamento geológico de CO<sub>2</sub>; Mudanças climáticas; Modelagem elétrica direta; Inversão de dados de resistividade elétrica.

## RESUMEN

SENSIBILIDAD DE LA INVERSIÓN ELÉCTRICA 1-D APLICADA A LA VIGILANCIA DEL ALMACENAMIENTO GEOLÓGICO DE CO<sub>2</sub>. Las discusiones sobre los efectos de las emisiones antropogénicas de gases de efecto invernadero y sus consecuencias sobre el cambio climático han ganado notoriedad pública en las últimas décadas. La captura de dióxido de carbono (CO<sub>2</sub>) de fuentes industriales y su

posterior almacenamiento en reservorios geológicos tiene el potencial de jugar un papel importante en la reducción de los efectos nocivos de las emisiones de CO<sub>2</sub> a la atmósfera en el mediano y largo plazo. Con base en sus propiedades físicas para la aplicación de técnicas geofísicas, el estudio y evaluación del comportamiento de las rocas en presencia de CO<sub>2</sub> ha demostrado alta relevancia. Este estudio aborda el monitoreo de reservorios geológicos en presencia de CO<sub>2</sub> a través del método de resistividad eléctrica para estimar las propiedades eléctricas de las rocas involucradas, como la saturación de CO<sub>2</sub> y la resistividad eléctrica del medio. Se realizaron simulaciones en un modelo sintético de cuatro capas. Los resultados validaron la aplicabilidad del método eléctrico en el monitoreo de la inyección y fuga de CO<sub>2</sub>.

*Palabras clave:* Almacenamiento geológico de CO<sub>2</sub>; Cambio climático; Modelado eléctrico directo; Inversión de datos de resistividad eléctrica.

## 1 INTRODUCTION

Global warming is one of humanity's significant challenges today. The main problem is the fact that CO<sub>2</sub> absorbs thermal infrared light, thus being the primary agent of the greenhouse effect. The harmful effects have encouraged the industry to reduce CO<sub>2</sub> emissions. CO<sub>2</sub> is generated by concentrated industrial activities, such as thermal power plants, fossil fuel extraction units, and other industrial processes that use combustion in general.

Although costly, one alternatives to mitigating the greenhouse effect is the geological storage of carbon, or CCS (Carbon Capture and Storage), which consists of storing CO<sub>2</sub> in appropriate sedimentary layers.

The geological formations that can be used for CO<sub>2</sub> storage are (i) deep saline aquifers, (ii) depleted or non-depleted oil and gas reservoirs, and (iii) coal layers. Subsurface fluids fill the pore spaces of the rock, as do water, oil, natural gas, and CO<sub>2</sub>. The purpose of CO<sub>2</sub> geological storage is its injection into porous rock formations (BENSON & COLE 2008). Geological storage is based on the principle of returning CO<sub>2</sub> underground. Therefore, CO<sub>2</sub> is stored in the lithosphere and its pore spaces.

In these formations, CO<sub>2</sub> can then be stored by different trapping mechanisms, depending on the relevant mechanism for the rock type. Among the three classes of geological formations, oil reservoirs are strong candidates for reducing CO<sub>2</sub> accumulation in the atmosphere due to the technological knowledge acquired by the oil industry. These reservoirs are proven geological traps, capable of retaining fluids and gases for a long time.

The CO<sub>2</sub> injection technique for EOR – Enhanced Oil Recovery has been a common practice in the oil industry for several decades and can be used in geological carbon storage. In reservoirs undergoing advanced recovery operations, storing a portion of the injected gas is a direct consequence of using CO<sub>2</sub> when the gas produced with the oil is captured and injected into the reservoir.

The objectives of monitoring geological CO<sub>2</sub> storage are to ensure storage integrity, to meet safety requirements for subsurface activities during and after the operational phase, and assess the injection process as planned in the intended formation. The primary safety hazards are the potential for leakage into the atmosphere or other geological formations, which could result in groundwater contamination.

Exploration geophysics is an essential tool in a CO<sub>2</sub> geological storage project, starting with the choice of target reservoirs for permanent CO<sub>2</sub> storage, and it is also important for monitoring its integrity. According to GASPERIKOVA & HOVERSTEN (2006), the viability of each geophysical technique depends on the magnitude of the measured contrast of the geophysical property produced by the increase in CO<sub>2</sub> concentration, and the resolution inherent in the method.

A secondary objective of the monitoring is to research and develop geological storage of CO<sub>2</sub> to better understand the physical and chemical processes in the reservoir. This process is essential for optimizing future storage (THOMAS & BENSON 2005).

Among the existing geophysical methods, exploration seismology is the most used, for target selection and monitoring. CO<sub>2</sub> injection and storage have in common that the stored CO<sub>2</sub> can be monitored by reflection seismology and well-

to-well seismic tomography (LAZARATOS & MARION 1997). Monitoring through the inversion of seismic data allows us to identify the formation of the CO<sub>2</sub> plume in negative contrast with the initial velocity field.

It is also possible to integrate exploration seismology with other methods. For example, HOVERSTEN et al. (2002) used the electromagnetic method and exploration seismology in the well-to-well tomography methodology, before and during CO<sub>2</sub> injection in southern California's Lost Hills oil field.

However, other methods should be preferably used in an integrated way during monitoring, such as the electromagnetic, gravimetric, and electrical methods. According to GASPERIKOVA & HOVERSTEN (2006), non-seismic methods have begun to be used as they are less expensive techniques.

CO<sub>2</sub> is resistive, so electrical methods are appropriate for brine-containing formations. For most depth ranges of interest for geological storage, CO<sub>2</sub> is less dense and more compressible than brine and oil. Thus, seismic and gravimetric methods are considerable options for brine or oil formations (GASPERIKOVA & HOVERSTEN 2006).

In the last 15 years, some CO<sub>2</sub> injection and monitoring projects have emerged in Brazil. Petrobras and IFP have initiated a joint research project on Carbon Capture Storage to determine the feasibility of CO<sub>2</sub> injection and underground storage in the Buracica oil field in Recôncavo Basin (DINO & LE GALLO 2007). The purpose of this study is to apply the performance assessment process, using the experimental design theory and the response surface methodology, to evaluate the suitability level of the method for establishing the practicability of CO<sub>2</sub> geological storage (ESTUBLIERA et al. 2011). Still in Brazil, ROUCHON et al. (2011) suggested several surface surveillance guidelines inspired by data from an EOR-CO<sub>2</sub> oil field case study where an extensive surface and reservoir gas survey has been performed. They also considered that the gases that may leak from a CO<sub>2</sub> geological storage could have a wide range of compositions as well as different fluxes of CO<sub>2</sub> with expected fluxes in worst-case leak scenarios, showing that both have comparable amplitudes.

Non-seismic methods, including electrical methods, have also been used in Brazil. OLIVA et al. (2018) presented results from a field experiment

in Santa Catarina using a 3-D electrical imaging technique to monitor CO<sub>2</sub> migration in saturated and unsaturated clay-rich sediments. Comparison of post-injection electrical imaging results with pre-injection images shows changes in resistivity values consistent with released CO<sub>2</sub> migration pathways.

In this study, we use a non-seismic method called electrical resistivity prospecting for monitoring CO<sub>2</sub> geological reservoirs. We consider a model of four parallel plane layers. The observed data are the apparent resistivity values as a function of different offsets between the current electrodes. Those values are the input for the inversion procedure. The inversion output is the values of layer resistivity and thickness. The data were corrupted with random noise to validate the methodology so that the RMS deviation between the apparent resistivity and the apparent resistivity with noise was around 5%. The simulation results validated the 1-D approach of the resistivity method, which showed sufficient sensitivity to evaluate the electrical properties of rocks involved in geological CO<sub>2</sub> storage.

## 2 ELECTRICAL PROPERTIES AND CO<sub>2</sub> MONITORING

The electrical resistivity of reservoir rocks is highly sensitive to variations in water saturation, according to Archie's equation (ARCHIE 1942)

$$\rho_{rock} = \frac{\rho_{brine}}{(1 - S_{gas})^2 \phi^2}, \quad (1)$$

where  $\rho_{rock}$  is the density of the rock as a function of gas saturation  $S_{gas}$ . On the other hand,  $S_{gas} = 1 - S_{water}$  in which  $S_{water}$  is the water saturation.  $\rho_{brine}$  is the resistivity of the fluid in the pores (in this case, brine). All petroleum fluids (oil, condensate, and gas) and CO<sub>2</sub> are electrically resistive, so Archie's equation is appropriate (GASPERIKOVA & HOVERSTEN 2006).

Archie's equation accurately describes the electrical resistivity of sedimentary rocks as a function of the listed parameters. It works well on clean and homogeneous sandstone. A critical factor in resistivity measurements is the clay content, which produces a low apparent resistivity compared to actual resistivity because clay minerals tend to improve the path for electrical currents. The resistivity values increase during the gas injection period, but when calculated by the Archie equation, they present a saturation of around

10%. This number is less than that estimated from neutron log data. Such low saturation is assumed to be the effect of clay inclusion in the reservoir (NAKATSUKA et al. 2010).

As CO<sub>2</sub> displaces water, the coupling coefficient decreases. On average, the observed coupling coefficients for constant gas flow are about ten times smaller than for water flow in the same sample. Since the coupling coefficient of liquid CO<sub>2</sub> is lower than that of water, the most effective way to monitor the spatial variation in the injected CO<sub>2</sub> flow is to monitor the forward front of the CO<sub>2</sub>/H<sub>2</sub>O ratio, where the coupling coefficient is more significant (HOVERSTEN & GASPERIKOVA 2005).

When the injected CO<sub>2</sub> reaches measurement zones, the resistivity increases considerably. The onset of increased resistivity indicates that CO<sub>2</sub> is migrating from the bottom to the upper end of the sandstone. The CO<sub>2</sub> migration pattern varies due to the permeability and mineral composition of the rocks. In the case of clean and homogeneous sandstone, the fluid migrates as a uniform front in a relatively short period due to the high permeability. In contrast, heterogeneity and clay content decrease the displacement rate and complicate the process.

Gas saturation can be estimated from the initial resistivity of the rock fully saturated with brine (before the injection) and the resistivity of the partially saturated rock brine (during the injection) with the following equation:

$$S_{CO_2} = 1 - \left( \frac{1}{RI} \right)^{\frac{1}{n}}, \quad (2)$$

where  $RI$  is called resistivity index and  $n$  is a numerical factor called saturation exponent. This empirical relationship was obtained through laboratory experiments on sandstone samples from different reservoirs (NAKATSUKA et al. 2010).  $RI$  is defined as the ratio between the resistivity at a given instant of time and the initial resistivity, i.e.  $RI = \rho / \rho_0$ , hence equation (2) can be written as:

$$S_{CO_2} = 1 - \left( \frac{\rho_0}{\rho} \right)^{\frac{1}{n}}. \quad (3)$$

Figure 1 shows the relationship between CO<sub>2</sub> saturation and the resistivity index  $RI$ , using the parameter  $n = 1.62$ , as suggested by SCHMIDT-HATTENBERGER et al. (2014).

The curve in figure 1 is generic for any value of  $\rho_0$ . If we consider  $\rho_0 = 100 \Omega.m$ , which corresponds to the resistivity of the rock 100%

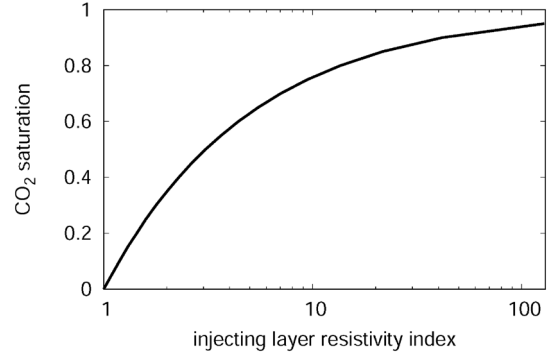


FIGURE 1 – CO<sub>2</sub> saturation curve as a function of the resistivity index, with the index  $n$  equal to 1.62.

saturated with brine, we can present a curve of absolute resistivity values, as shown in figure 2.

On one hand, if  $RI = 1.0$ , it follows that  $\rho = \rho_0$  and the saturation is zero ( $S_{CO_2} = 0$ ), corresponding to the curve's origin. On the other hand, a 95% saturation corresponds to  $RI = 128.14$ , i.e.  $\rho = 12,814 \Omega.m$ . Moreover, figure 2, which is specific for  $\rho_0 = 100 \Omega.m$ , indicates the dynamics of the CO<sub>2</sub> injection process through arrows.

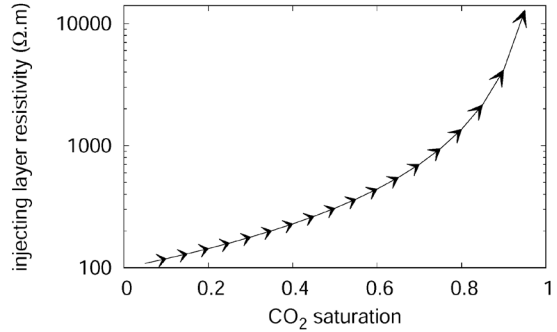


FIGURE 2 – Absolute resistivity values as a function of CO<sub>2</sub> saturation, for  $\rho_0 = 100 \Omega.m$ , which corresponds to the rock resistivity 100% saturated with brine. The arrows indicate the dynamics of the CO<sub>2</sub> injection process, with the final value  $\rho = 12,814 \Omega.m$  corresponding to a 95% CO<sub>2</sub> saturation.

### 3 FORWARD MODELING AND INVERSION OF 1-D ELECTRICAL RESISTIVITY DATA

Electrical resistivity sounding is a subsurface mapping technique that analyzes electrical properties in a horizontal layered model. It allows the location of bodies that generate anomalous responses in the measurement equipment. The method has been applied in mineral exploration,

underground water exploration, geotechnical engineering, environmental geophysics, and archeology. The maximum depth limit is about 1 km (KEAREY et al. 2002).

The electrical resistivity method requires electrodes in direct contact with the Earth's surface. An electric current produced by the equipment is injected into the soil through an electrode  $A$  with a return through another electrode  $B$ . The potential difference from this current is measured at two other electrodes,  $M$  and  $N$ . The inverse procedure estimates the anomaly source, which uses apparent resistivity values as input data. The apparent resistivity, in turn, is calculated as a function of the spacing or offset between electrodes and uses the measured values of electric current and potential difference.

The potential measured at the electrode  $M$  ( $V_M$ ) will present contributions due to the potentials generated by  $A$  and  $B$  ( $V_A$  and  $V_B$ ). The same is valid for the electrode  $N$ . In this sense, the difference  $\Delta V = V_M - V_N$  is expressed by:

$$\Delta V = \frac{I\rho}{2\pi} \left[ \left( \frac{1}{AM} - \frac{1}{BM} \right) - \left( \frac{1}{AN} - \frac{1}{BN} \right) \right], \quad (4)$$

where  $AM$ ,  $AN$ ,  $BM$  and  $BN$  are the spacing or offset between the electrodes. By isolating the resistivity, we obtain the following:

$$\rho = \frac{\Delta V}{I} \frac{2\pi}{\left( \frac{1}{AM} - \frac{1}{BM} \right) - \left( \frac{1}{AN} - \frac{1}{BN} \right)} = K \frac{\Delta V}{I}. \quad (5)$$

The parameter  $K$  is called the geometric array factor.

If we consider a single surface current electrode in a uniform medium, the current will flow radially, with a uniform current distribution over hemispherical shells in the half-space. These shells are the equipotential surfaces. Expression (5) measures and computes the electrical resistivity of a homogeneous half-space using a generic four-electrode arrangement. The resistivity value will be constant regardless of the spacing between the electrodes.

To conduct a Schlumberger survey, one has that que  $MN = 2l$  and  $AB = 2L$ , so that, after some approximations, the geometric factor is given as  $K = \pi L^2/2l$ , which implies

$$\rho = \frac{\pi L^2}{2l} \frac{\Delta V}{I}. \quad (6)$$

Equation (6) is specific to a homogeneous medium. If the subsurface is non-homogeneous, the resistivity will be a position of space, meaning that the value obtained from equation (6) will have a contribution from all subsurface resistivity values. Therefore, the apparent resistivity function is not constant, and the field-measured values of  $\Delta V$  and  $I$ , for different spacing  $l$  and  $L$ , will provide a set of apparent resistivity values denoted by  $\rho^a$ .

For the forward modeling step, consider a model with  $NL$  flat horizontal layers, thicknesses  $h_i$  and layer resistivities  $\rho_i$  with  $i = 1, \dots, LN$ . A current is injected into the surface layer. For a Schlumberger survey, the apparent resistivity is expressed by (KELLER & FRISCHKNECHT 1966, INMAN 1975):

$$\rho^a = \rho_1 L^2 \int_0^\infty k_{ii}(\lambda) J_1(\lambda L) \lambda d\lambda, \quad i = 1, \dots, LN, \quad (7)$$

where the auxiliary function  $k_{ii}(\lambda)$  is expressed as:

$$k_{ii}(\lambda) = \frac{1 - \mu_{ii} \exp(-2\lambda h_i)}{1 + \mu_{ii} \exp(-2\lambda h_i)}, \quad i = 1, \dots, LN, \quad (8)$$

with

$$\mu_{ii} = \frac{\rho_1 - \rho_2 k_{2,i+1}}{\rho_1 + \rho_2 k_{2,i+1}}, \quad i = 1, \dots, LN. \quad (9)$$

The process continues until the final layer, which is the homogeneous half-space. The results are:

$$k_{NL-1,NL}(\lambda) = \frac{1 - \mu_{NL-1,NL} \exp(-2\lambda h_{NL-1})}{1 + \mu_{NL-1,NL} \exp(-2\lambda h_{NL-1})}, \quad (10)$$

with

$$\mu_{NL-1,NL} = \frac{\rho_{NL-1} - \rho_{NL}}{\rho_{NL-1} + \rho_{NL}}. \quad (11)$$

The above equations can be synthesized into the compact expression  $\mathbf{d} = \mathbf{g}(\mathbf{m})$ , where the vector  $\mathbf{d}$  contains the apparent resistivities  $\rho^a$ . In the inverse procedure both the layer resistivities and thicknesses are unknown. Thus, the layer resistivities  $\rho_i$  and layer thicknesses  $h_i$  form the vector  $\mathbf{m}$ , to be estimated. The inverse problem is non-linear, so an approximation is required to linearize the problem, usually the Taylor's expansion. The vector  $\mathbf{d}$  is expanded around a neighborhood of  $\mathbf{m}$ , denoted by  $\mathbf{m}^0$ :

$$\mathbf{d} = \mathbf{g}(\mathbf{m}) = \mathbf{d}^0 + \left. \frac{\partial \mathbf{g}(\mathbf{m})}{\partial \mathbf{m}} \right|_{\mathbf{m}=\mathbf{m}^0} (\mathbf{m} - \mathbf{m}^0) + \dots \quad (12)$$

where  $\mathbf{d}^0 = \mathbf{g}(\mathbf{m}^0)$ . Truncating the Taylor's series at the first order, we have

$$\Delta \mathbf{d} = \mathbf{G} \Delta \mathbf{m}, \quad (13)$$

where  $\Delta \mathbf{d} = \mathbf{d} - \mathbf{d}^0$ ,  $\Delta \mathbf{m} = \mathbf{m} - \mathbf{m}^0$  and the elements of the matrix  $\mathbf{G}$  are calculated numerically by the expression:

$$G_{ij} = \left. \frac{\partial g_i(m_j)}{\partial m_j} \right|_{m_j=m_j^0}. \quad (14)$$

Equation (13) can be generalized as:

$$\Delta \mathbf{d}^k = \mathbf{G}^k \Delta \mathbf{m}^k, \quad (15)$$

where  $\Delta \mathbf{d}^k = \mathbf{d}^{obs} - \mathbf{d}^k$  and  $\Delta \mathbf{m}^k = \mathbf{m}^{k+1} - \mathbf{m}^k$ . Moreover, the elements of matrix  $\mathbf{G}^k$  in equation (15) are calculated numerically for each iteration by the expression:

$$G_{ij}^k = \left. \frac{\partial g_i(m_j)}{\partial m_j} \right|_{m_j=m_j^k}. \quad (16)$$

The matrix in equation (15) is then inverted, for example, by the generalized inverse,

$$\Delta \mathbf{m}^k = (\mathbf{G}^k)^+ \Delta \mathbf{d}^k, \quad (17)$$

and the solution is updated iteratively by the expression

$$\mathbf{m}^{k+1} = \Delta \mathbf{m}^k + \mathbf{m}^k. \quad (18)$$

As a rule,  $\mathbf{G}^k$  is not a square matrix. Furthermore, there are usually more equations (or data) than unknowns (or parameters), i.e., the inverse problem is said to be overdetermined. Therefore, the solution expressed by equation (17) can be extended by using the least squares method:

$$\mathbf{m}^{k+1} = (\mathbf{G}^{T,k} \mathbf{G}^k)^+ \mathbf{G}^{T,k} \Delta \mathbf{d}^k + \mathbf{m}^k. \quad (19)$$

Sometimes, the square matrix  $\mathbf{G}^{T,k} \mathbf{G}^k$  may not be a complete rank, so damping is necessary. This variant of least squares is called damped least squares:

$$\mathbf{m}^{k+1} = (\mathbf{G}^{T,k} \mathbf{G}^k + \varepsilon^2 \mathbf{I})^+ \mathbf{G}^{T,k} \Delta \mathbf{d}^k + \mathbf{m}^k. \quad (20)$$

The literature suggests techniques for choosing the non-negative damping factor  $\varepsilon^2$ . However, in this study, the choice of  $\varepsilon^2$  was made by trial and error.

## 4 SIMULATIONS AND RESULTS

Several simulations were performed on subsurface layered models using a 1-D approach. The results provide interpretations in a single dimension, in this case, along the depth axis.

We employed the linearized inversion method described by INMAN et al. (1973) to estimate the model parameters (layer resistivities and layer thicknesses). In the present study, we applied the damped least squares method for the inversion, as proposed by INMAN (1975). This method mitigates the ill-conditioned problem by damping the main diagonal of the matrix to be inverted, which is also sometimes called zeroth-order regularization. For the numerical procedure of the inversion, we used the decomposition by singular values.

The inversion process is ambiguous as it can provide solutions where the conductance (the product between the thickness and the conductivity of a given layer) is constant. In contrast, the individual thickness and/or conductivity values may vary.

The Schlumberger arrangement was chosen for this study due to its widespread use. We considered a four-layer model, with layers labeled A, B, C, and D, from the uppermost to the lowest layer, with thicknesses equal to 50 m. The layer resistivities, from top to bottom, are 50, 100, 50, and 200  $\Omega \cdot \text{m}$ .

Layer B, with  $\rho_0 = 100 \Omega \cdot \text{m}$ , initially saturated with 100% brine, characterizes the pre-injection condition. The solid curve of figure 3 illustrates the apparent resistivity of this model. The gradual injection of  $\text{CO}_2$  in layer B will imply a change in the apparent resistivity curve. Figure 3 depicts two additional curves representing the intermediate condition (with 50%  $\text{CO}_2$  injection and 50% brine) and the post-injection condition (95%  $\text{CO}_2$  injection and 5% brine).

The inversion was performed using the previously described algorithm. The observed data vector consisted of 15 values of apparent resistivity. The model parameters vector has seven components: 4-layer resistivity and 3-layer thickness values. Note that the fourth and last layer has a semi-infinite thickness. Therefore, the inverse problem is overdetermined. The vector of true model parameters is expressed as follows:

$$\mathbf{m}^{true} = (\rho_1, \rho_2, \rho_3, \rho_4, \Delta z_1, \Delta z_2, \Delta z_3). \quad (21)$$

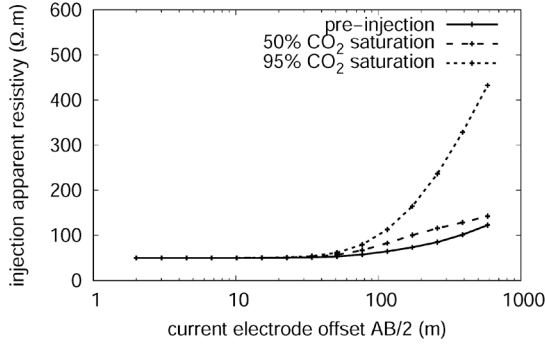


FIGURE 3 – Apparent resistivity as a function of distance due to CO<sub>2</sub> injection in layer B, with  $\rho_0 = 100 \Omega.m$ . The solid curve describes the pre-injection condition, with 100% brine. The dashed curve represents the intermediate condition, with 50% CO<sub>2</sub> injection and 50% brine. The dotted curve depicts the post-injection condition, with 95% CO<sub>2</sub> injection and 5% brine.

In the first series of simulations, we utilized noise-free data. We required an a priori estimate of the model parameters to perform the inversion. For this case, a priori model consisted of resistivity values equivalent to 80% of the true model and thickness values equal to the true values. Table 1 presents the true and a priori layer resistivity values for this and subsequent stages.

TABLE 1 – True and a priori values of layer resistivity (in  $\Omega.m$ ) for CO<sub>2</sub> injection (upper panel) and leakage (lower panel) processes.

CO <sub>2</sub> injection in layer B						
Layer	0% CO <sub>2</sub>		50% CO <sub>2</sub>		95% CO <sub>2</sub>	
	$\rho^{true}$	$\rho^{prior}$	$\rho^{true}$	$\rho^{prior}$	$\rho^{true}$	$\rho^{prior}$
A	50	40	50	40	50	40
B	100	80	307	246	12814	10251
C	50	40	50	40	50	40
D	200	160	200	160	200	160

CO <sub>2</sub> leakage in layer C						
Layer	95% CO <sub>2</sub>		50% CO <sub>2</sub>		0% CO <sub>2</sub>	
	$\rho^{true}$	$\rho^{prior}$	$\rho^{true}$	$\rho^{prior}$	$\rho^{true}$	$\rho^{prior}$
A	50	40	50	40	50	40
B	100	80	100	80	100	80
C	6407	5125	154	123	50	40
D	200	160	200	160	200	160

Figure 4 displays three profiles corresponding to the pre-injection condition: the true model in red, the a priori model in blue, and the estimated

model in black. The recovered model is virtually equal to the true model in terms of resistivity and thickness values.

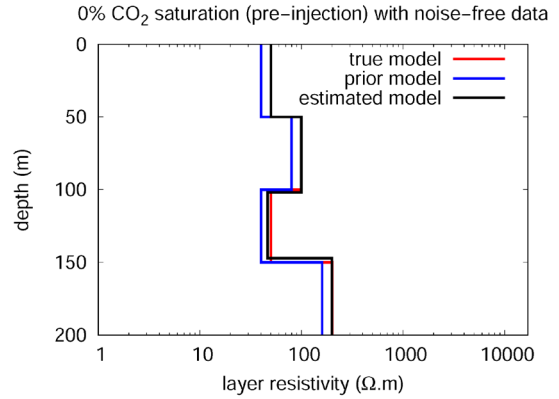


FIGURE 4 – Inversion of noise-free apparent resistivity data in the pre-injection condition of CO<sub>2</sub>, with layer B saturated with 100% brine. The red profile represents the true model, the blue demonstrates the a priori model, and the black indicates the estimated model.

Evaluating the proximity between the prior and true models in each simulation is essential. For this purpose, we employed the RMS estimator of deviation between the true values of the model parameter  $\mathbf{m}^{true}$  and the corresponding a priori values  $\mathbf{m}^{prior}$ :

$$\varepsilon_{rms}^{prior} = \frac{\sqrt{\sum_{i=1}^7 (m_i^{prior} - m_i^{true})^2}}{\sqrt{\sum_{i=1}^7 (m_i^{true})^2}} \times 100\%, \quad (22)$$

in which we obtained  $\varepsilon_{rms}^{prior} = 3.52\%$  in the pre-injection condition.

Similarly, for calculating the RMS deviation between the true model parameters  $\mathbf{m}^{true}$  and the estimated model parameters  $\mathbf{m}^{est}$ , we used the following estimator:

$$\varepsilon_{rms}^{est} = \frac{\sqrt{\sum_{i=1}^7 (m_i^{est} - m_i^{true})^2}}{\sqrt{\sum_{i=1}^7 (m_i^{true})^2}} \times 100\%, \quad (23)$$

in which we obtained the value  $\varepsilon_{rms}^{est} = 0.06\%$  for the pre-injection condition. Table 2 contains the simulation results for the various injection stages.

TABLE 2 – Simulation results of the processes of CO<sub>2</sub> injection (upper panel) and leakage (lower panel). Deviation of prior information is calculated using equation (22), while the estimated model error is calculated using equation (23).

	Stage	A priori $\varepsilon_{rms}^{prior}$ (%)	Noise-free data $\varepsilon_{rms}^{est}$ (%)	Noisy data $\varepsilon_{rms}^{est}$ (%)
CO <sub>2</sub> injection in layer B	0% saturation (pre-injection)	3.52	0.06	0.90
	50% saturation	3.80	0.37	0.19
	95% saturation	4.00	0.89	0.80
CO <sub>2</sub> leakage in layer C	95% saturation (pre-leakage)	4.00	0.69	0.81
	50% saturation	3.66	0.21	0.14
	0% saturation	3.52	0.06	0.90

By maintaining the same proportion between resistivities to define the a priori information, the inversion proved satisfactory in the intermediate condition, with 50% CO<sub>2</sub> injection and 50% brine in layer B. Figure 5 depicts the three curves. For this condition, the estimators provided  $\varepsilon_{rms}^{prior} = 3.80\%$  and  $\varepsilon_{rms}^{est} = 0.37\%$ .

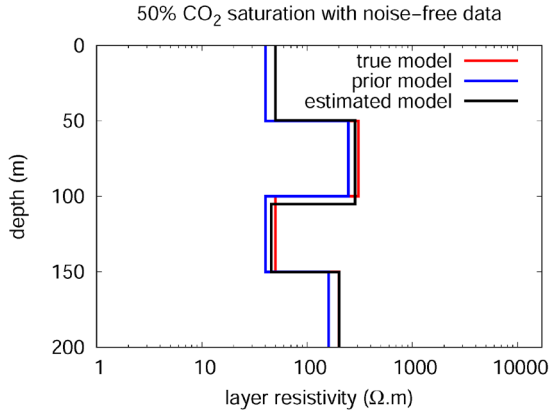


FIGURE 5 – Inversion of noise-free apparent resistivity data in the intermediate condition, with 50% CO<sub>2</sub> injection and 50% brine in layer B. The red profile represents the true model, whereas the blue demonstrates the a priori model, and the black indicates the estimated.

Finally, figure 6 displays the result of inverting the apparent resistivity data post-injection, with 95% CO<sub>2</sub> injection and 5% brine in layer B. Once again, we can see that the estimated model closely matches the real model. In this final condition, the estimators provided  $\varepsilon_{rms}^{prior} = 4.00\%$  and  $\varepsilon_{rms}^{est} = 0.89\%$ .

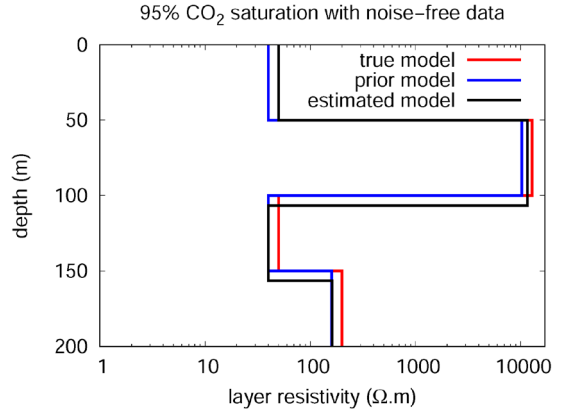


FIGURE 6 – Inversion of noise-free apparent resistivity data post-injection, with 95% CO<sub>2</sub> injection and 5% brine in layer B. The red profile represents the true model, the blue demonstrates the a priori model, and the black indicates the estimated model.

Figures 4, 5, and 6 can be integrated, as shown in figure 7, which illustrates the three stages of the process simultaneously: pre-injection, intermediate, and final. Figure 7(a) provides the true models, and figure 7(b) presents the estimated models. There, we can observe that layer A is accurately recovered in terms of resistivity and thickness, and layer B is recovered in terms of resistivity. However, a slight error is present in the thickness of layer B, which propagates into the recovery of model parameters of layers C and D.

For methodology validation purposes, we introduced random noise to the apparent resistivity  $\rho^a$  in the following formula:

$$\rho_i^{a,*} = \rho_i^a + ar_i \rho_i^a, \quad i = 1, \dots, M, \quad (24)$$



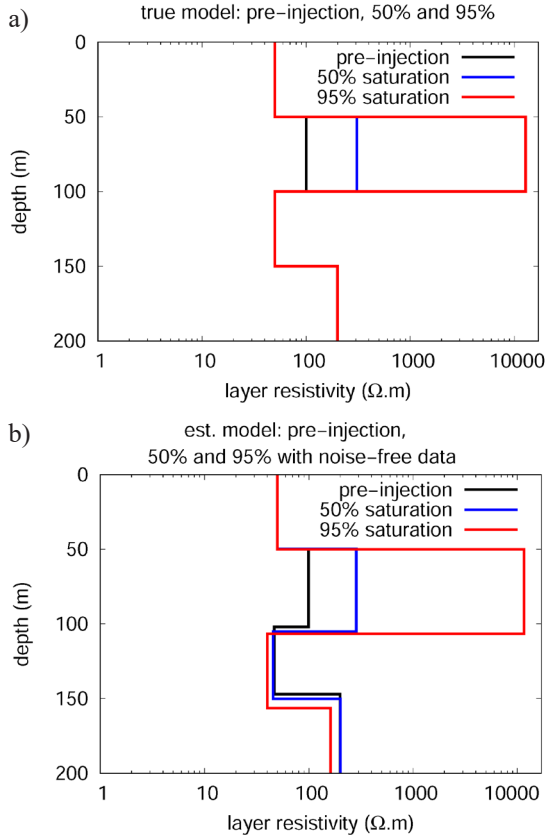


FIGURE 7 – Different stages of CO<sub>2</sub> injection with noise-free data: pre-injection (black), intermediate (blue), and final (red). Figure 7(a) displays true models and figure 7(b) presents estimated models.

in which  $\rho^{a,*}$  is the apparent resistivity contaminated with noise;  $\alpha$  is the noise factor and  $r_i$  represents the random sequence. The value of  $\alpha$  was chosen to ensure that the RMS deviation  $\varepsilon_{rms}^{noise}$  between  $\rho^{a,*}$  and  $\rho^a$  is approximately 5%. This RMS estimator is expressed as follows:

$$\varepsilon_{rms}^{noise} = \frac{\sqrt{\sum_{i=1}^M (\rho_i^{a,*} - \rho_i^a)^2}}{\sqrt{\sum_{i=1}^M (\rho_i^a)^2}} \times 100\%. \quad (25)$$

Figure 8 illustrates the apparent resistivity curves of  $\rho^a$  and  $\rho_i^{a,*}$ . The electrode spacing was limited to 100 m to enhance the visibility of noise-induced fluctuations.

Noisy resistivity values  $\rho_i^{a,*}$  were used as input data for the inversion procedure. Figure 9 demonstrates the result in the CO<sub>2</sub> pre-injection condition, with layer B saturated with 100% brine. The RMS deviation between the true model and the a priori model remains unchanged compared

to the noise-free case, i.e.,  $\varepsilon_{rms}^{prior} = 3.52\%$ . However, as expected, the RMS deviation between the true model and the estimated model increased from  $\varepsilon_{rms}^{est} = 0.06\%$  to  $\varepsilon_{rms}^{est} = 0.90\%$  due to the presence of noise.

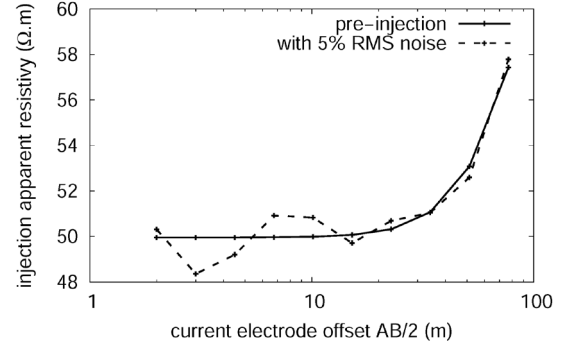


FIGURE 8 – Curves of apparent resistivity  $\rho^a$  and noise-contaminated apparent resistivity  $\rho^{a,*}$ . The RMS deviation between the two curves is  $\varepsilon_{rms}^{noise} = 5\%$ . The noise-caused fluctuation becomes more noticeable with the electrode spacing limited up to 100 m.

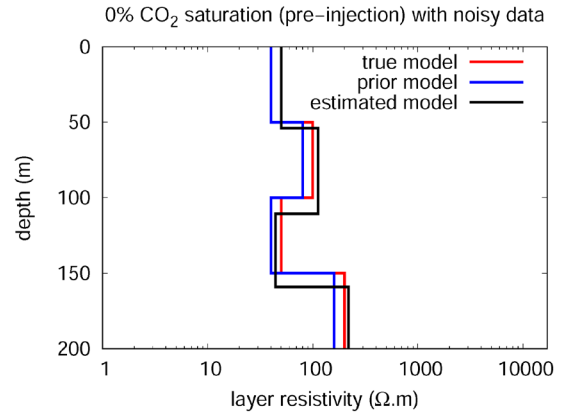


FIGURE 9 – Inversion of apparent resistivity noisy data in the pre-injection condition, with layer B saturated with 100% brine. The red curve represents the true model, the blue curve illustrates the a priori model, and the black curve indicates the estimated model.

Figure 10 displays the inversion result with noisy data for the intermediate condition, with 50% CO<sub>2</sub> injection and 50% brine. Once again, the RMS deviation between the true model and the a priori remains the same as in the noise-free case ( $\varepsilon_{rms}^{prior} = 3.80\%$ ). Interestingly, the RMS deviation between the true and estimated model decreased from  $\varepsilon_{rms}^{est} = 0.37\%$  to  $\varepsilon_{rms}^{est} = 0.19\%$ .

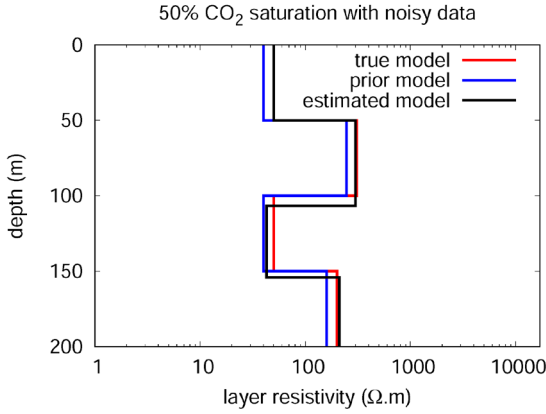


FIGURE 10 – Inversion of apparent resistivity noisy data in the intermediate condition, with 50% CO<sub>2</sub> injection and 50% brine in layer B. The red curve represents the true model, the blue curve illustrates the a priori model, and the black curve indicates the estimated model.

Figure 11 exhibits the simulation for the final stage (post-injection condition), with 95% CO<sub>2</sub> injection and 5% brine in the same layer. In this final condition, the estimators provided  $\varepsilon_{rms}^{prior} = 4.00\%$  and  $\varepsilon_{rms}^{est} = 0.89\%$ .

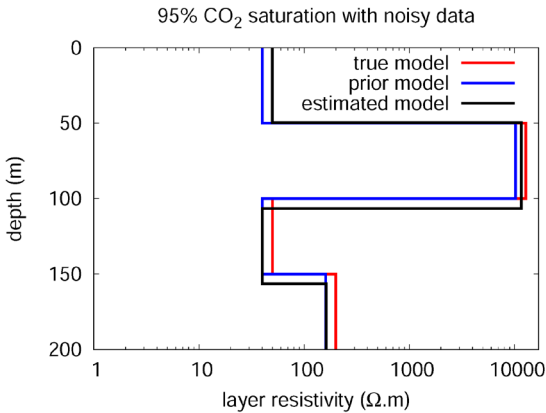


FIGURE 11 – Inversion of apparent resistivity noisy data post-injection, with 95% CO<sub>2</sub> injection and 5% brine in layer B. The red curve represents the true model, the blue curve illustrates the a priori model, and the black curve indicates the estimated model.

Despite the presence of noise, the results were quite satisfactory. As figure 12 indicates, we integrated the different CO<sub>2</sub> injection stages in the case of the noise-free simulations.

The second set of simulations describes the CO<sub>2</sub> leaking condition, in which the brine replaces the CO<sub>2</sub>. Using the same four-layer model, we now

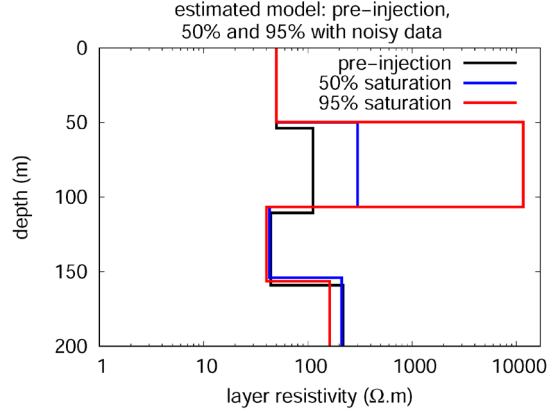


FIGURE 12 – Estimated models at different stages of CO<sub>2</sub> injection: pre-injection (black curve), intermediate (blue curve), and final (red curve).

consider that the leakage occurs in layer C instead of layer B. We examined CO<sub>2</sub> saturation of 95%, 50% and 0%, with the complementary values summing up to 100% representing the brine saturation.

We consider the reference value of  $\rho_0 = 6406.76 \Omega.m$  as the resistivity of layer C saturated with 95% CO<sub>2</sub>. Figure 13 presents the absolute resistivity values, in which the arrows indicate the CO<sub>2</sub> leakage dynamics. In the final leakage step, with 0% CO<sub>2</sub> saturation, we have  $\rho_0 = 50 \Omega.m$ .

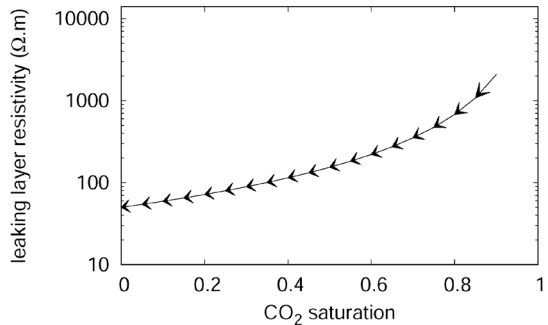


FIGURE 13 – Absolute resistivity values as a function of CO<sub>2</sub> saturation, in which  $\rho_0 = 6406.76 \Omega.m$  corresponds to the resistivity of rock saturated with 95% CO<sub>2</sub>. The arrows indicate the dynamics of the CO<sub>2</sub> leakage process, with the final value  $\rho_0 = 50 \Omega.m$ .

Figure 14 depicts the apparent resistivity curves. The solid curve represents the pre-leakage condition. The dashed curve illustrates the apparent resistivity in the intermediate condition, with 50% CO<sub>2</sub> injection and 50% brine. The dotted curve corresponds to the final condition of total CO<sub>2</sub> leakage, with 100% brine.

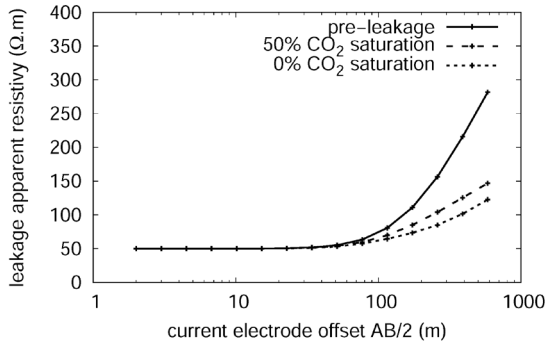


FIGURE 14 – Change in apparent resistivity due to CO<sub>2</sub> leakage in layer C, with  $\rho_0 = 6406.76 \Omega.m$ . The solid curve depicts the pre-leakage condition, with the layer saturated with 95% CO<sub>2</sub>. The dashed curve describes the intermediate condition, with 50% CO<sub>2</sub> injection and 50% brine. The dotted curve describes the post-leakage condition, with 100% brine.

Figure 15 presents the inversion result of the apparent resistivity data in the pre-leakage condition. We applied the same criterion of a priori information in the injection process, with resistivity values equivalent to 80% of the true layer resistivity. In contrast, a priori thickness values are equal to true values.

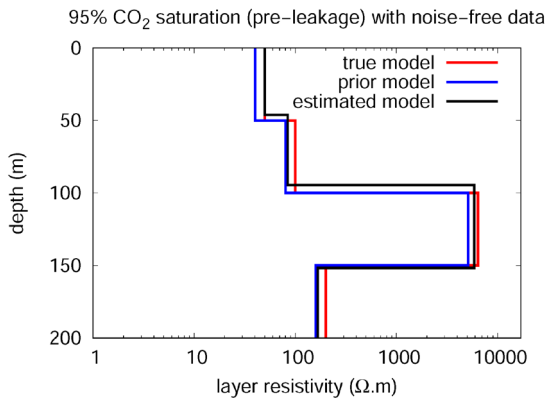


FIGURE 15 – Inversion of apparent resistivity noise-free data in the pre-leakage condition, with 95% CO<sub>2</sub> injection and 5% brine in layer C. The red curve represents the true model, the blue curve illustrates the a priori model, and the black curve indicates the estimated model.

Figure 16 depicts the inversion of apparent resistivity data in the leakage condition, with 50% CO<sub>2</sub> injection and 50% brine in layer C. The red curve represents the true model, the blue curve illustrates the a priori model, and the black curve indicates the estimated model.

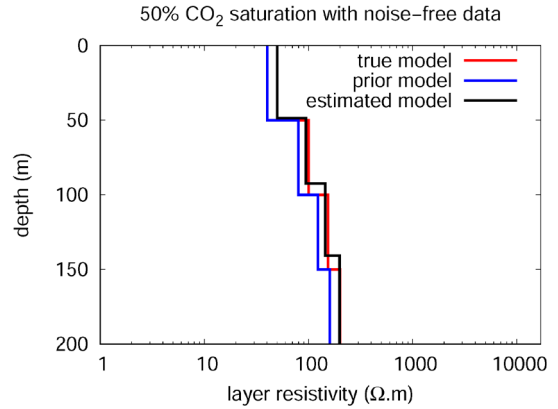


FIGURE 16 – Inversion of apparent resistivity noise-free data in the leakage condition, with 50% CO<sub>2</sub> injection and 50% brine in layer C. The red curve represents the true model, the blue curve illustrates the a priori model, and the black curve indicates the estimated model.

The result of inverting the final stage of leakage is not displayed since it is equivalent to the result of figure 9, which is the initial stage of the injection process.

Figure 17(a) presents the integration of the different stages of CO<sub>2</sub> leakage for the true models, while figure 17(b) depicts the integration for the estimated models.

We also incorporated random noise in the leakage process. Figure 18 illustrates the inversion of the apparent resistivity data in the pre-leakage condition, using the same a priori information criterion as in the noise-free simulation. Despite the presence of noise, the estimated model remains very close to the true model. In quantitative terms, the RMS deviation between the true model and the estimated model, which was  $\epsilon_{rms}^{est} = 0.69\%$  for the noise-free case, increased to  $\epsilon_{rms}^{est} = 0.81\%$ .

Figure 19 presents the result of inverting the intermediate stage of leakage with the presence of noise. Interestingly, as observed in the CO<sub>2</sub> injection process, the RMS deviation between the true and estimated models decreased from  $\epsilon_{rms}^{est} = 0.21\%$  in the noise-free data case to  $\epsilon_{rms}^{est} = 0.14\%$  in the noisy data case.

Inverting the final stage of the leakage process would yield the same result as the initial stage of the injection process (Figure 15). Finally, figure 20 demonstrates the integration of the different stages of CO<sub>2</sub> leakage with the presence of noise.

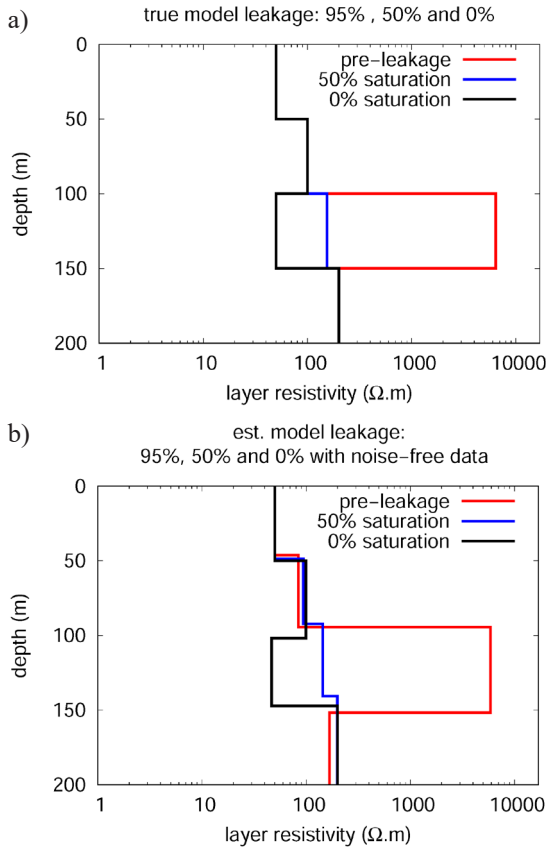


FIGURE 17 – Different stages of CO<sub>2</sub> leakage without adding noise: pre-leakage (black curve), intermediate (blue curve), and final (red curve). Figure 17(a) depicts the true models, while figure 17(b) displays the estimated models.

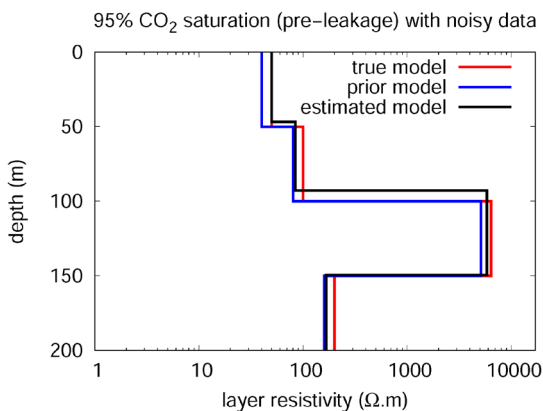


FIGURE 18 – Inversion of apparent resistivity noisy data in the pre-leakage condition, with 95% CO<sub>2</sub> injection and 5% brine in layer C. The red curve represents the true model, the blue curve illustrates the a priori model, and the black curve indicates the estimated model.

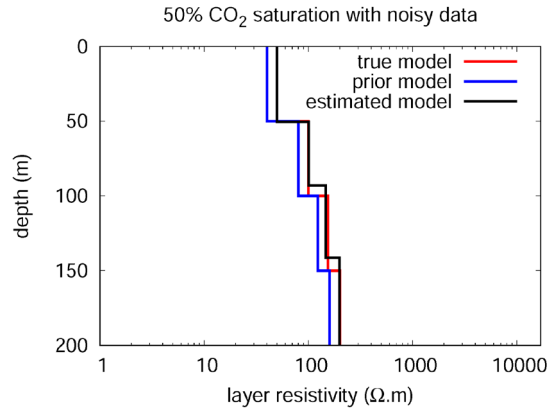


FIGURE 19 – Inversion of apparent resistivity data without adding noise in the post-injection condition, with 50% CO<sub>2</sub> injection and 50% brine in layer C. The red curve represents the true model, the blue curve illustrates the a priori model, and the black curve indicates the estimated.

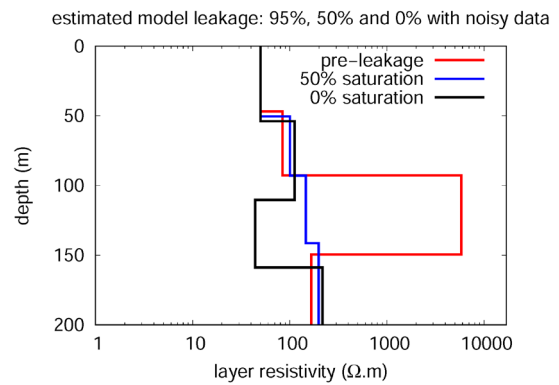


FIGURE 20 – Estimated models of the different stages of CO<sub>2</sub> leakage with noise: pre-leakage (red curve), intermediate (blue curve) and final (black curve).

## 5 CONCLUSIONS

In this study, we verified the applicability of 1-D electrical modeling and inversion to monitor CO<sub>2</sub> storage. By measuring resistivity differences before, during, and after gas injection, it is possible to monitor the gas dynamics in the subsurface. The simulation results in a four-layer model, including the presence of noise, aligned with our expectations, as evidenced by the overlapping curves of the injection or leakage in the different stages. With the presence of CO<sub>2</sub>, the resistivity curve becomes more accentuated due to its higher resistance than other pore-filling fluids, such as water. Despite the limitation of the 1-D approach and the fact that we do not consider any CO<sub>2</sub> dynamic process,

except the resistivity variation with CO<sub>2</sub> saturation, the proposed methodology has been validated. It proves its applicability to CO<sub>2</sub> geological storage, which offers a viable alternative to mitigate the environmental impacts of CO<sub>2</sub> emissions.

## 6 ACKNOWLEDGEMENTS

The author thanks the Conselho Nacional de Desenvolvimento Científico e Tecnológico (CNPq) for funding the Instituto Nacional de Ciência e Tecnologia de Geofísica do Petróleo (INCT-GP). He also thanks the anonymous reviewers of Derbyana for their suggestions that improved the manuscript.

## 7 REFERENCES

- ARCHIE, G. 1942. The electrical resistivity log as an aid in determining some reservoir characteristics. *Transactions of the AIME*, 146: 54-62. <https://doi.org/10.2118/942054-G>
- BENSON, S.M.; COLE, D.R. 2008. CO<sub>2</sub> sequestration in deep sedimentary formations. *Elements*, 4: 325-331. <https://doi.org/10.2113/gselements.4.5.325>
- DINO, R.; LE GALLO, Y. 2009. CCS Project in Recôncavo Basin. *Energy Procedia*, 1(1): 2005–2011. <https://doi.org/10.1016/j.egypro.2009.01.261>
- ESTUBLIERA, A.; DINO, R.; SCHINELLI, M.C.; BARROUX, C.; BELTRAN, A.M. 2011. CO<sub>2</sub> injection in Buracica - Long-term performance assessment. *Energy Procedia*, 4: 4028–4035. <https://doi.org/10.1016/j.egypro.2011.02.344>
- GASPERIKOVA, E.; HOVERSTEN, G.M. 2006. A feasibility study of nonseismic geophysical methods for monitoring geologic CO<sub>2</sub> sequestration. *The Leading Edge*, 25(10): 1282–1288. <https://doi.org/10.1190/1.2360621>
- HOVERSTEN, G.M.; GASPERIKOVA, E. 2005. Non-seismic geophysical approaches to monitoring. In: D.C. Thomas & S.M. Benson (ed.) *Carbon Dioxide Capture for Storage in Deep Geologic Formations*. Amsterdam, Elsevier, vol. 2, Chapter 23, p. 1071-1112.
- HOVERSTEN, G.M.; GRITTO, R.; WASHBOURNE, J.; DALEY, T. 2002. *CO<sub>2</sub> gas/oil ratio prediction in a multi-component reservoir by combined seismic and electromagnetic imaging*. Lawrence Berkeley National Laboratory. <http://www.escholarship.org/uc/item/0d65c9b1>
- INMAN, J.R. 1975. Resistivity inversion with ridge regression. *Geophysics*, 40(5): 798-817. <https://doi.org/10.1190/1.1440569>
- INMAN, J.R.; RYU, J.; WARD, S.H. 1973. Resistivity inversion. *Geophysics*, 38(6): 1088-1108. <https://doi.org/10.1190/1.1440398>
- KEAREY, P.; BROOKS, M.; HILL, I. 2002. *An Introduction to Geophysical Exploration*. Wiley-Blackwell, London, 3<sup>rd</sup> ed., 272 p.
- KELLER, G.V.; FRISCHKNECHT, F.C. 1966. *Electrical Methods in Geophysical Prospecting*. Pergamon, London, 526 p.
- LAZARATOS, S.K.; MARION, B.P. 1997. Crosswell seismic imaging of reservoir changes caused by CO<sub>2</sub> injection. *The Leading Edge*, 16(9):1300-1308. <https://doi.org/10.1190/1.1437788>
- NAKATSUKA, Y.; XUE, Z.; GARCIA, H.; MATSUOKA, T. 2010. Experimental study on CO<sub>2</sub> monitoring and quantification of stored CO<sub>2</sub> in saline formations using resistivity measurements. *International Journal of Greenhouse Gas Control*, 4(2): 209-216. <https://doi.org/10.1016/j.ijggc.2010.01.001>
- OLIVA, A.; KIANG, C.H.; MELO, C.L.; BRESSAN, L.W.; GOUDINHO, F.S.; CONSTANT, M.J.; ROCHA, H.R.; NAKAEMA, W.M.; ROSÁRIO, F.; MUSSE, A.P.S. 2018. Geoelectrical Remote System for Monitoring Shallow Subsurface CO<sub>2</sub> Migration. In: INTERNATIONAL CONFERENCE ON GREENHOUSE GAS CONTROL TECHNOLOGIES, 14, Melbourne, *Proceedings*, 1-12.
- ROUCHON, V.; MAGNIER, C.; MILLER, D.; BANDEIRA, C.; GONÇALVES, R.; DINO, R. 2011. The relationship between CO<sub>2</sub> flux and gas composition in soils above an EOR-CO<sub>2</sub> oil field (Brazil): a guideline


for the surveillance of CO<sub>2</sub> storage sites. *Energy Procedia*, 4: 3354–3362. <https://doi.org/10.1016/j.egypro.2011.02.257>

SCHMIDT-HATTENBERGER, C.; BERGMANN, P.; LABITZKE, T.; WAGNER, F. 2014. CO<sub>2</sub> migration monitoring by means of electrical resistivity tomography (ERT) - Review on five years of operation of a permanent ERT system at the Ketzin pilot site. *Energy*

*Procedia*, 63: 4366-4373. <https://doi.org/10.1016/j.egypro.2014.11.471>

THOMAS, D.C.; BENSON, S.M. 2005. *Carbon Dioxide Capture for Storage in Deep Geologic Formations-Results from the CO<sub>2</sub> Capture Project: Vol 1 -Capture and Separation of Carbon Dioxide from Combustion; Vol. 2, Geologic Storage of Carbon Dioxide with Monitoring and Verification*, Elsevier, Amsterdam.

*Author's address:*

Amin Bassrei\* ( 0000-0002-4653-2016) – Centro de Pesquisa em Geofísica e Geologia, Universidade Federal da Bahia e Instituto Nacional de Ciência e Tecnologia de Geofísica do Petróleo, Instituto de Geociências, Rua Barão de Jeremoabo, s/n, Campus Universitário de Ondina, CEP 40170-115, Salvador, BA, Brazil. *E-mail:* [bassrei@ufba.br](mailto:bassrei@ufba.br)

\* Correspondent author

*Manuscript submitted on 28 July 2024, accepted on 5 October 2024.*

